Influence of Hydrothermal Parameters on Photocatalytic Activity of $BiVO_4$ for Degradation of Methylene Blue

Vinh-Tien Truong[1,2], Pham-Ngoc-My Le[1,2], and Minh-Vien Le[1,2*]

[1]*Faculty of Chemical Engineering, Ho Chi Minh City University of Technology (HCMUT), 268 Ly Thuong Kiet Street, District 10, Ho Chi Minh City 700000, Vietnam*

[2]*Vietnam National University Ho Chi Minh City, Linh Trung Ward, Thu Duc District, Ho Chi Minh City 720325, Vietnam*

* ***Corresponding author:***

email: lmvien@hcmut.edu.vn

Received: September 14, 2024
Accepted: December 6, 2024

DOI: 10.22146/ijc.99923

Abstract: *A facile hydrothermal method has been developed to improve the intrinsic photocatalytic activity of $BiVO_4$. By assessing the effects of three key hydrothermal parameters (temperature, time, and pH levels) on catalytic performance, optimal conditions for maximizing photocatalytic activity were identified. Characterization through XRD, FE-SEM, and UV-DRS demonstrates the crucial role of the (040) facet and reduced non-uniform compressive strain in enhancing the photocatalytic activity of bismuth vanadate. The sample synthesized at 200 °C, pH 1, with 10 h of hydrothermal treatment shows significant decolorization of methylene blue with a comparable rate constant. This study presents a promising approach to synthesizing high-performance photocatalysts through a straightforward synthesis process without the use of directing agents.*

Keywords: *$BiVO_4$; hydrothermal synthesis; Le Bail fit; MB degradation; multifaceted geometry*

■ INTRODUCTION

The global population is projected to surge from 22 to 34% by 2050 [1], which can lead to many challenges. According to the United Nations World Water Development Report (2018 edition), approximately 6.0 billion people may lack access to clean water by mid-century. Anthropogenic and industrial activities have exacerbated this crisis by discharging non-biodegradable compounds directly into aquatic ecosystems. Notably, the textile industry contributing to 7% of the world's total exports [2], discharges dyes into water bodies. These chromophoric compounds ruin the aesthetic appeal of aquatic environments and disrupt the ecological balance. Specifically, methylene blue (MB) is a popular cationic dye with the chemical formula $C_{16}H_{18}N_3SCl$. It is odorless, soluble in water at room temperature, and usually used as a colorant for paper, silk, textiles, cosmetics, and pharmaceutical industries. Long-term exposure to MB could cause various health problems, such as nausea, vomiting, mental confusion, or even cancer [3].

To address these issues, sustainable strategies for contaminant removals are imperative. Advanced oxidation processes (AOPs) emerge as promising methods for eliminating organic pollutants and converting them into innocuous byproducts - carbon dioxide, water, and other fragments. In AOPs, using heterogeneous photocatalysts is a well-established strategy as it can harness solar energy and be separated easily from the post-treatment suspension. Metal oxides, particularly titanium oxide (TiO_2), have dominated photocatalytic research for decades. However, TiO_2 is only reactive under UV light, utilizing only 4% of available solar energy, significantly limiting its application [4]. Extensive effort has been made to develop photocatalysts driven by visible light for wastewater treatment. Bismuth vanadate ($BiVO_4$) is a more affordable alternative [5], offering various advantages such as non-toxicity, good dispersibility, chemical and physical stability [6]. $BiVO_4$ naturally exists in three distinct crystalline phases: orthorhombic pucherite, tetragonal dreyerite, and monoclinic clinobisvanite. Among these, the monoclinic phase stands out as the most active candidate in photocatalysis, primarily owing

to its narrow bandgap energy of 2.4 eV [6]. Moreover, some studies indicate that $BiVO_4$ has a lower effective mass of charge carriers than certain commercial semiconductors such as TiO_2 [7]. A lower effective mass means better performance because the charge carriers can move more freely and effectively participate in the reactions before recombining. The unique overlap of O 2p and Bi 6s orbitals in the valence band enhances the mobility of photogenerated charge carriers, resulting in improved photocatalytic activity [8]. This makes $BiVO_4$ a compelling candidate for sustainable water treatment.

Recent efforts to enhance the photocatalytic activity of $BiVO_4$ involve creating composites [9-11], doped materials [12], and metal-loaded materials [13]. However, these modified materials exhibit improved photocatalytic performance over pristine $BiVO_4$ but complex synthesis. Facet engineering, with diverse morphologies including truncated hexagonal bipyramid [6], leaf-like [14], sheet-like [15], and flakes-stacked structure [16], has emerged as a promising approach to enhance the inherent qualities of $BiVO_4$ but requires co-solvent or directing agents such as EDTA [6], $TiCl_3$ [15], SDBS [16], CTAC [17], and CTAB [18], which may leave residues on the catalyst surface [17]. These reports highlighted the importance of morphology in photocatalysis. Spherical particles were less effective in photodetoxification of levofloxacin (42.3%) compared to truncated-bipyramidal counterparts (71.2%) [19]. Enhanced photoactivity is due to facet isotype heterojunctions between (040) and (110) facets, with a high ratio benefiting photocatalysis [20]. More importantly, facet engineering facilitates photo-redox reactions on different crystal facets [21], driven by band edge level discrepancies, creating an energetic gradient that aids charge separation [22].

Crystal morphology can be controlled using surfactants or directing agents, but it is primarily governed by the kinetics of crystal growth. Hydrothermal synthesis, which alters the solubility of nearly all inorganic materials, is a popular method for producing well-crystallized materials by recrystallizing materials from high-temperature aqueous solutions under high pressure. Since no directing agents are used, the composition of the hydrothermally treated mixture, which is strongly influenced by hydrothermal parameters, becomes crucial. Recent research has focused on the effects of pH level on crystal morphology as it directly influences dissolution, recrystallization process, and crystal orientation [23]. Additionally, the duration of hydrothermal treatment was reported to govern the amount of monoclinic phase and crystal size [24]. However, the impact of hydrothermal temperature has received less attention. A recent study showed that the hydrothermal temperature influences the growth rate of crystals along specific directions, determining their orientation [25]. Moreover, temperature-induced microstructural changes also affect photocatalytic activity [26], but there is limited research on $BiVO_4$. Therefore, this study aims to investigate the effect of all three key hydrothermal parameters on the photocatalytic activity of $BiVO_4$. Alongside determining an optimal synthesis condition for generating effective photocatalysts in the degradation of organic pollutants, this study analyzes structural and morphological transformation in the resulting samples using the X-ray diffraction (XRD) technique and field emission scanning electron microscope (FESEM), respectively. The light absorption characteristic of $BiVO_4$ is also accessed via an up-to-date analytic method using ultraviolet-diffuse reflectance spectra (UV-DRS).

■ EXPERIMENTAL SECTION

Materials

Bismuth(III) nitrate ($Bi_5O(OH)_9(NO_3)_4$, 98%) and ammonium metavanadate (NH_4VO_3, 99%) were commercially available from Merck-Germany and Himedia-India, respectively. Ammonium hydroxide (NH_4OH, 25–28 wt.%), nitric acid (HNO_3, 68 wt.%), and MB ($C_{16}H_{18}ClN_3S$, 98.5%) were purchased from Xilong, China. All reagents were of analytical grade and directly used without further purification.

Instrumentation

The phase composition and crystal structure of $BiVO_4$ have been investigated by using room temperature XRD on a D2 Phaser – Bruker diffractometer using CuK_α radiation with 2θ range of

20°–80° and the scan rate of 0.2°/s. The morphology of the synthesized materials was characterized by a FESEM (Hitachi S4800). The UV-DRS were recorded using a UV–visible spectrophotometer (JASCO V-550, Japan).

Procedure

Synthesis of multifaceted $BiVO_4$

In a typical synthesis, 2.0 mmol of $Bi_5O(OH)_4(NO_3)_9$ and 10.0 mmol NH_4VO_3 were dissolved in 60.0 mL of 2.0 mol L^{-1} HNO_3 solution. After obtaining a clear solution, the pH of the solution was adjusted to 1.0 with NH_4OH solution (25–28 wt.%). The obtained light-yellow suspension was vigorously stirred for 2 h before transferring to a 100 mL Teflon-lined-stainless steel autoclave. The hydrothermal reaction was conducted at 473 K in the oven for 10 h. Following, the autoclave was allowed to cool naturally to ambient temperature. The yellow precipitate was separated, washed with distilled water, and dried under high vacuum conditions (ca. 500 mbar) at 80 °C.

The effects of three variables (temperature, duration of hydrothermal treatment, and pH level) were examined in the following experimental protocol. Initially, three samples were synthesized at varying temperatures: 150, 200, and 220 °C, each with the same pH level of 0.50 and the treatment duration of 10 h. Once a suitable temperature producing the most active materials was identified, the influence of treatment duration was assessed by creating samples with the processing time of 6, 10, and 24 h. Finally, the pH factor was evaluated by modifying the pH level of the suspension before hydrothermal treatment to values ranging from 0.25 to 3.00.

Photocatalytic performance test

The experiments were conducted using a double shell batch reactor and a 26 W simulated sunlight lamp (Exo-Terra) as a light excitation source (Fig. S3, provided in Supporting Information (SI)) to examine the photocatalytic decomposition performance of the fabricated $BiVO_4$. The illuminance was about 1700 lx, measured by a digital lux meter (model YF-1065). The experimental procedure commenced by stirring the mixture of MB solution and the catalyst for 60 min in the absence of illumination. This initial step is to ensure the establishment of adsorption/desorption equilibrium. This experiment used 200 mL of 10 ppm MB solution and a catalyst dose of 1 g L^{-1}. During illumination, 5 mL aliquots were withdrawn at 30-min intervals and were filtered by a 0.22 µm microfilter to remove solid particles. Subsequently, the absorbance was quantified at the wavelength of 664 nm using UV-vis HITACHI U-2910 spectrophotometer.

A 10 ppm MB solution was prepared to evaluate the self-degradation of MB. One 200 mL portion was left in the dark, while another 200 mL portion was adjusted to 12 pH level by gradually adding NaOH solution dropwise (the volume negligibly changed). The light absorbance (A) was measured after the pH adjustment. The solution obtained was exposed to a 26 W simulated sunlight lamp (Exo-Terra) without any photocatalyst. The light absorbance was recorded at regular intervals, and the self-degradation percentage was estimated as A_t/A_0.

■ RESULTS AND DISCUSSION

The Effect of Hydrothermal Temperature

The impact of hydrothermal temperature on the characteristics of $BiVO_4$ was evaluated through three samples, which were prepared under an identical pH level but varied temperatures (150 °C, Fig. 1(a), 200 °C, Fig. 1(b), and 220 °C, Fig. 1(c)). Their XRD diffraction patterns contain characteristic peaks corresponding to monoclinic phase $BiVO_4$ (JCPDS 14-0688). In addition, these peaks at 2θ of 18.7°, 18.9°, 28.6°, 28.8°, 28.9°, 30.5°, 34.5°, and 35.2° correspond to (110), (11$\bar{1}$), (130), (021), (22$\bar{1}$), (040), (200) and (20$\bar{2}$) planes of monoclinic $BiVO_4$ (m-$BiVO_4$), respectively (Fig. 1).

Recent studies have shown that the reduction and oxidation reactions primarily take place on the (040) and (110) crystal facets of $BiVO_4$, respectively, resulting in improved electron-hole separation. It is thus important to monitor the ratio between (040) and (110) facets, which can be observed through XRD peak intensities, I_{040}/I_{110}. It has been reported that $BiVO_4$ with a high ratio of I_{040}/I_{110} = 11.2 could enhance the water oxidation activity because a more exposed (040) facet is proposed

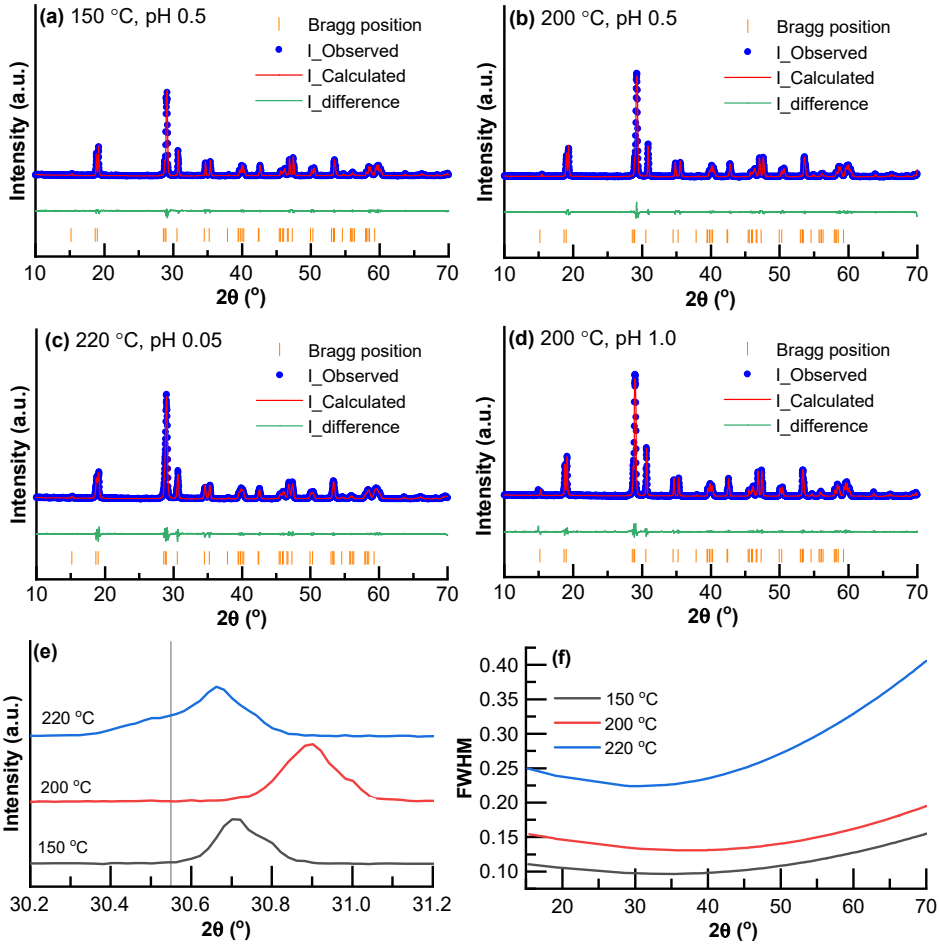

Fig 1. (a–c) Le Bail fit of XRD patterns of samples prepared at different temperatures (150, 200, and 220 °C) and (d) the optimal sample (200 °C, pH 1.0, 10 h); (e) peak shift phenomenon in XRD patterns; f) dependence of FWHM on diffraction angles

to possess superior water molecule adsorption and provide more active sites ($BiVO_4$), which is more facile for the multi-electrons transfer involved in water oxidation reaction [15]. Furthermore, an increased exposure factor of the (040) facet positively influences charge separation and anti-recombination in (040)/(110) isotype heterojunctions, resulting in enhanced photocatalytic activity [19]. However, an equal fraction of these exposed facets, achieved using NaCl as a morphology-controlling agent, was determined to maximize the charge separation efficiency in the photocatalytic coupling of formaldehyde [27]. Therefore, while a high ratio of (040)/(110) is beneficial for photocatalytic performance, its optimal value is contingent upon the specific reaction context. In this study, the ratio I_{040}/I_{110} increased from 1.26 to 1.33 as the temperature rose from 150 to 200°°C and dropped to 1.13 when the temperature reached 220°°C. Intriguingly, at 200 °C, the multifaceted structure was preserved with an increase in I_{040}/I_{110} when the pH level changed from 0.5 (Fig. 1(c)) to 1.0 (Fig. 1(d)). This unequivocally demonstrated that multifaceted $BiVO_4$ crystals with varying extents of (040) and (110) facets were synthesized.

Moreover, the dominance of a specific crystal plane ($h_ik_il_i$) can be quantified by the texture coefficients $p(h_ik_il_i)$ [28]. The deviation of p(hkl) from unity reflects the degree to which a particular crystallographic plane is favored over the bulk material.

$$p(h_ik_il_i) = \frac{I(h_ik_il_i)}{I'(h_ik_il_i)}\left[\frac{1}{N}\sum_{i=1}^{N}\frac{I(h_ik_il_i)}{I'(h_ik_il_i)}\right]^{-1} \quad (1)$$

Table 1. Variation of the texture coefficient p(hkl) due to hydrothermal temperatures (150, 200, and 220 °C)

(hkl)	150 °C	200 °C	220 °C
(110)	0.98	0.82	0.92
(11$\bar{1}$)	1.27	1.12	1.10
(021)	0.84	0.98	1.05
(22$\bar{1}$)	0.94	1.03	0.96
(040)	1.11	1.27	1.14
(200)	1.19	1.17	1.01
(20$\bar{2}$)	1.12	1.04	1.02

In Eq. (1), $I(h_ik_il_i)$ and $I'(h_ik_il_i)$ are the intensities of the diffraction peaks of the planes $(h_ik_il_i)$ in the sample under investigation and a randomly oriented sample (obtained from JCPDS card) respectively, and N represents the total number of considered diffraction peaks (here, N = 7 for this analysis). The multifaceted geometry (or polyhedral shape) is confirmed by data presented in Table 1, as certain planes exhibit p(hkl) values greater than 1.0 [29]. Notably, the dominance of plane (040) at 150 °C was not apparent. However, its significance surged at 200°C. This phenomenon might be attributed to the influence of temperature on the formation of $BiVO_4$ particles, which comprise dissolution and recrystallization. The growth rate of each facet varies depending on the temperature [25]. An increase in temperature accelerates the growth speed in all directions. Other facets shrink before the (040) plane because the growth speed of $BiVO_4$ in the [010] direction is the slowest [25]. When the temperature continues rising to 220 °C, the dissolution process becomes faster, forming additional growth units (nucleation sites). This, in turn, limits crystal orientation and decreases granularity [30]. Additionally, the heat from the system supplies more energy for crystals to continue growing in the [010] direction [25]. Consequently, overheating leads to a decline in the proportion of the (040) facet. Nonetheless, the facet (040) retained its dominance at 220 °C, albeit with a reduced p(hkl) value relative to the sample prepared at 200 °C. This was consistent with the changes in the intensity ratio of (040) to (110), which represents the relative extent of (040) and (110) planes.

Another important consideration is the shift of peak positions in diffraction patterns. Fig. 1(e) visually demonstrates that the diffraction peaks for all samples are located at higher angles than the standard positions. Applying Bragg's law ($2d\sin\theta = n\lambda$): compressive strain, which potentially diminishes the interspacing distance (d) is inferred to cause the observed shift of diffraction peaks toward higher angles (θ). Consequently, the lattices experienced compressive strain during synthesis.

Ideally, a crystal would develop uniformly in all directions; however, no single crystal is perfect due to its size. The broadening of XRD peaks indicates deviations from ideal crystallinity, primarily caused by crystallite size and lattice strain. The crystallite size refers to the coherently diffracting domain, while lattice strain originates from lattice defects, such as point defects or dislocations. The lattices in the vicinity of defects are elastically distorted (or strained). This distortion causes the broadening of the diffraction peaks [31], as evident in the diffraction pattern of the sample subjected to hydrothermal treatment at 220 °C. This phenomenon arises from non-uniform lattice distortions. The degree of variation in the lattice constants and lattice dislocations, collectively contribute to the lattice strain. Notably, the lattice strain can be exploited to modulate the properties of metal oxide semiconductors, although its effects have received limited attention [32]. A previous study revealed that the compressive strain can reduce the bandgap but lowers the conduction band edge level, which is unfavorable for photocatalytic reduction reaction [26]. Thus, analyzing lattice strain is essential as it provides insights into lattice distortion as well as its impact on material catalytic performance.

Assessment of lattice strain typically relies on peak breadth, determined from simulated diffraction models. The experimental diffraction data was modeled using the Le Bail method with HighScore Plus software. The line profiles were modeled by the pseudo-Voigt function. Fig. 1(a-c) illustrates subtle changes in $I_{difference} = I_{observed} - I_{calculated}$, validating the model's effectiveness. Additionally, Goodness-of-fit $\chi^2 = (R_{wp} \times R^{-1}_{exp})^2$ is usually used as a metric to evaluate the refinement results [33]. None of χ^2 values are larger than threshold 5, which is commonly used as the maximum appreciable value for a good fitting to be

considered [34]. Furthermore, Fig. 1(f) illustrates the angular dependence of FWHM follows Caglioti's function as Eq. (2):

$$(\mathrm{FWHM})^2 = \mathrm{U}\tan^2\theta + \mathrm{V}\tan\theta + \mathrm{W} \quad (2)$$

U, V, and W are constants obtained from the refinement results. It is obvious that increasing the hydrothermal temperature exacerbates the peak broadening.

There are many analytical methods for evaluating these two factors (domain size and lattice strain) affecting XRD patterns. This study employed the classical Williamson-Hall method (Uniform Deformation Model (UDM)) and its modified versions (Uniform Stress Deformation Model (USDM), and Uniform Deformation Energy Density Model (UDEDM)), and the Halder-Wagner method to analyze microstructural changes in as-prepared samples through XRD patterns. The linear regression models used in these analytical methods are illustrated in Fig. 2. Detailed descriptions and the linear model parameters are provided in Supporting Information.

Regarding the classical Williamson-Hall method (UDM), it assumes uniform deformation throughout crystals. Some research suggests that a negative slope signifies compressive strain (−ε) in the sample, whereas a positive value indicates tensile strain (+ε) [35]. Table 2 shows that compressive strain is present in both samples prepared at 150 and 200 °C and it intensifies with increasing hydrothermal temperature. However, the positive slope for the sample fabricated at 220 °C (Fig. 2(a)) suggested the presence of tensile strain (+ε) [36],

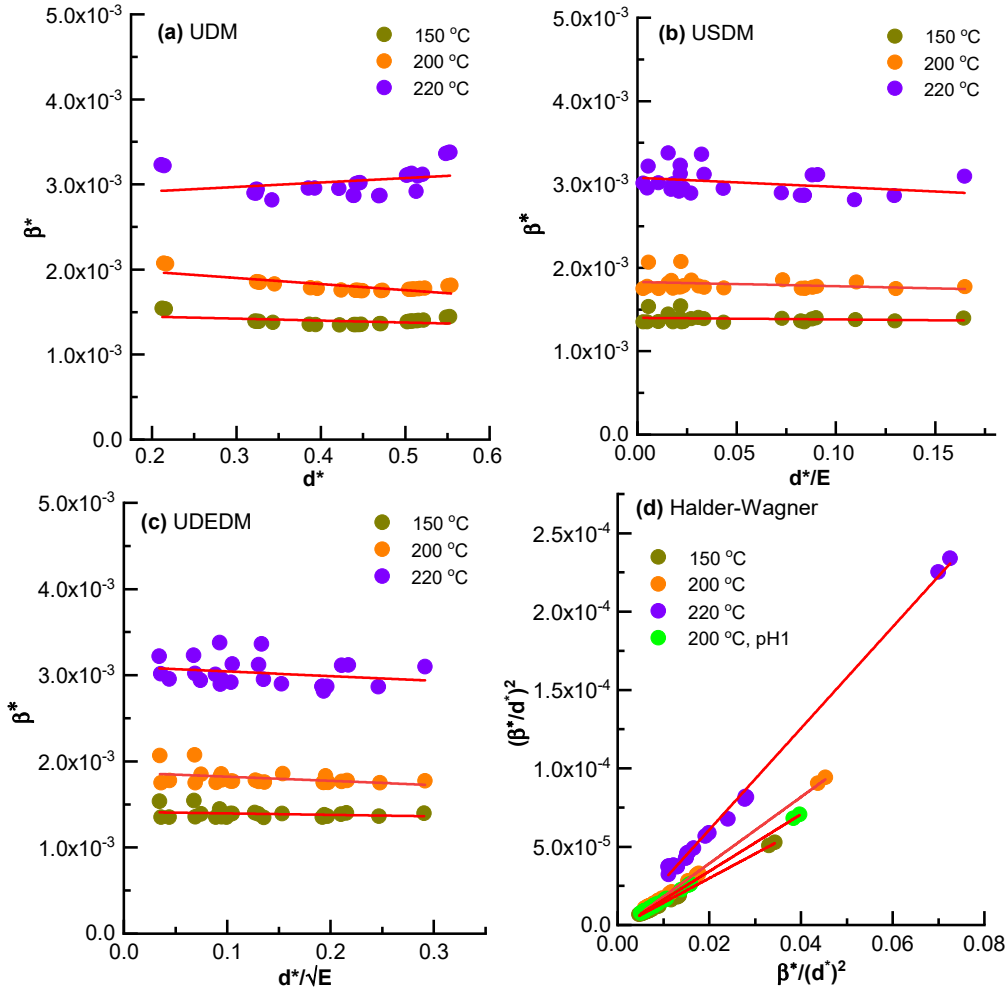

Fig 2. Analysis of peak broadening phenomenon in XRD patterns of the samples prepared at different hydrothermal temperatures using (a) UDM, (b) USDM, (c) UDEDM, and (d) Halder-Wagner models

Table 2. Lattice strain and domain size of samples prepared at different temperatures, determined by classical Williamson-Hall (UDM) and its modified versions (USDM, UDEDM), also the Halder-Wagner method

Temp. (°C)	Lattice strain ($\varepsilon.10^4$)			Optimal	Domain size (D [Å])			Optimal
	150	200	220		150	200	220	
UDM	−1.14	−3.59	2.60	–	666.67	476.19	357.14	–
USDM, ε along (040)	−0.30	−0.44	−1.76	–	714.29	555.56	322.58	–
UDEDM, ε along (040)	−0.49	−1.37	−1.53	–	714.29	526.32	322.58	–
Halder-Wager	−4.65	−7.04	−7.84	−5.67	641.03	471.69	309.59	549.45

which contradicts the prediction based on peak positions. In real crystals, the hypothesized isotropic nature of lattice strain in UDM can not be completely satisfied. Modified Williamson-Hall models have been developed to address this limitation. USDM and UDEDM consider non-uniform strain varying by crystallographic directions, while the stress (σ) and deformation energy density (u) are uniform in crystals. The strain ε is proportional to both σ and u by Young's modulus values (E(hkl)). The stationary value of Young's modulus was determined to reach the bottom in the direction (040) (Table 3), maximizing lattice strain along this axis. Both linear regression models of USDM (Fig. 2(b)) and UDEDM (Fig. 2(c)) posse negative slopes, indicating the existence of compressive strain in all samples. Notably, the linear fitting quality of these Williamson-Hall models suffers due to exceedingly small R^2 values (Table S4). This may be due to the implicit assumption in these models that diffraction profiles follow a Lorentzian function, which is inappropriate in this context as the diffraction profiles in these samples show good fitting with the Voigtian function, a convolution of Lorentzian and Gaussian functions. It is essential to note that the Williamson-Hall plots should not be used quantitatively beyond a first approximation [37]. However, they provide valuable insights into the nature of lattice strain (compressive strain) in crystals. In contrast, the Halder-Wagner method assumes line profiles adhere to Voigtian function, where the Lorentzian and Gaussian components arise solely to size and strain effects, respectively. This model yielded better fitting quality (Fig. 2(d)) and predicted a similar trend in compressive strain but with higher magnitude compared to USDM and UDEDM models (Table 2). Once again, these results confirm the existence of compressive strain in crystals prepared by this method and its correlation with the hydrothermal temperature.

Table 3. Stationary values of Young's modulus correspond to crystallographic directions

hkl	150 °C	200 °C	220 °C
(110)	9.73	9.74	9.74
$(11\bar{1})$	39.01	39.01	39.03
(021)	11.98	11.98	11.99
$(22\bar{1})$	19.19	19.19	19.20
(040)	3.13	3.13	3.13
(200)	16.69	16.69	16.70
$(20\bar{2})$	80.08	80.08	80.10

Regarding the domain size (D), these models predicted a similar trend: increasing hydrothermal temperature results in a smaller domain size. The low heating rate prolongs the dissolving span, causing a slower crystallization process and the formation of larger particles. When the temperature rises, the dissolution process accelerates, generating additional growth units (nucleation sites) that do not have enough time to fully develop, ultimately leading to smaller domain sizes [25]. Furthermore, Young modulus E(hkl) in modified Williamson-Hall models is usually used to evaluate the mechanical strength of materials. Lower E(hkl) indicates weaker interatomic strength [38]. Table 3 reveals that E(hkl) variation is minimal within this temperature range, with the lowest values in (040) and (110) directions. This suggests that the lattice structure along these orientations is particularly susceptible to deformation, especially at 200 and 220 °C. Rising temperature breaks domain structures, releasing an additional strain and reducing domain size [38]. The 220 °C sample shows pronounced peak broadening, which signifies more severe dislocation, disconnection, impurities, etc. [39]. In addition, the dislocation density, demoted as δ (where $\delta = D^{-2}$), is inversely proportional

to the domain size [40]. Consequently, smaller domains at higher temperatures lead to more dislocations, reducing charge separation efficiency [41-42].

Unit cells with the standard space group C2/c are retrieved from XRD refinement. The hydrothermal temperature above 150 °C significantly contracted lattice volume (Table S1). Notably, the smaller (larger) cell volume results in a smaller (larger) band gap [43]. It was reported that lattice cells could be contracted by external pressure [32] and expanded due to thermal expansion [44]. Within the scope of this study, it can be inferred that unit cells primarily contracted due to hydrothermal pressure between 150 and 200 °C. At 220 °C, thermal expansion surpassed compression from hydrothermal pressure. The transformation of lattice cells also influenced the lengths of V–O and Bi–O bonds. Table S2 shows that the shortest V–O and Bi–O bonds are at 200 °C, corresponding to the smallest unit cell volume. Shorter metal-oxygen bonds enhance hybridization [32]. Additionally, the valence band of $BiVO_4$ results from a hybrid of Bi 6s and O 2p orbitals [8]. Consequently, greater overlap between Bi 6s and O 2p orbitals can enhance the migration of photogenerated holes [8], which reduces recombination losses. Therefore, the sample prepared at 200 °C likely performs better phototactically.

The Effect of Synthesis pH on Morphology

In facet engineering, crystal morphology plays a crucial role in determining the photocatalytic performance of materials. Notably, the pH level during synthesis significantly impacts crystal shape. Bismuth precursor undergoes hydrolysis when dissolved in an aqueous environment, as described by Eq. (3) and (4) [45]. An acidic environment can effectively prevent the formation of high polymer forms $[Bi_nO_n]^{n+}$, which result from the reaction between Bi^{3+} ions and OH^- ions in alkaline conditions, subsequently dissolving to generate impurity Bi_2O_3 [45]. Moreover, the high concentration of H^+ inhibits the formation of slightly soluble $BiONO_3$, hence limiting the generation of kinetically favored tetragonal phase $BiVO_4$ (Eq. (5)). During hydrothermal treatment, this tetragonal phase transforms into the monoclinic phase through dissolution and recrystallization processes. While the nucleation is facilitated at higher pH levels, the dissolution rate of tetragonal particles is decreased, thereby slowing down the phase transition speed [23]. Besides, crystal growth occurs more rapidly in a higher pH environment, negatively impacting crystal orientation [23]. Small monoclinic grains emerge from the tetragonal particles, growing outward from the surface. Eventually, these grains coalesce, resulting in irregular shapes.

$$Bi^{3+} + 2H_2O \leftrightarrow Bi(OH)_2^+ + 2H^+ \quad (3)$$

$$NO_3^- + Bi(OH)_2^+ \leftrightarrow BiONO_3 \downarrow + H_2O \quad (4)$$

$$BiONO_3 + VO_3^- \rightarrow BiVO_4 \downarrow + NO_3^- \quad (5)$$

Fig. 3 illustrates the correlation between the pH level and the crystal morphology. It confirms that samples prepared at the pH level of 0.50 (Fig. 3(a)) and 1.0 (Fig. 3(b)) possessed uniformly smooth surfaces and polyhedral shapes, while the sample synthesized at the pH value of 2.0 had a superficial resemblance to "rod-like" shape (Fig. 3(c)). Besides, Fig. S7 demonstrates how the color of powder samples varies with different pH levels, suggesting alterations in light absorption [46].

The Optical Properties

The interaction between material and light is crucial for applications in photocatalytic processes. One essential factor affecting the optical characteristics of solids

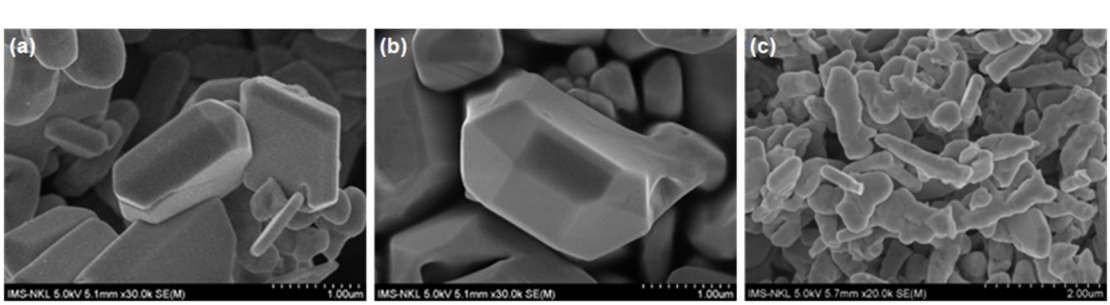

Fig 3. FE-SEM images of $BiVO_4$ crystals prepared at different pH values: (a) pH 0.5, (b) pH 1.0, (c) pH 2.0

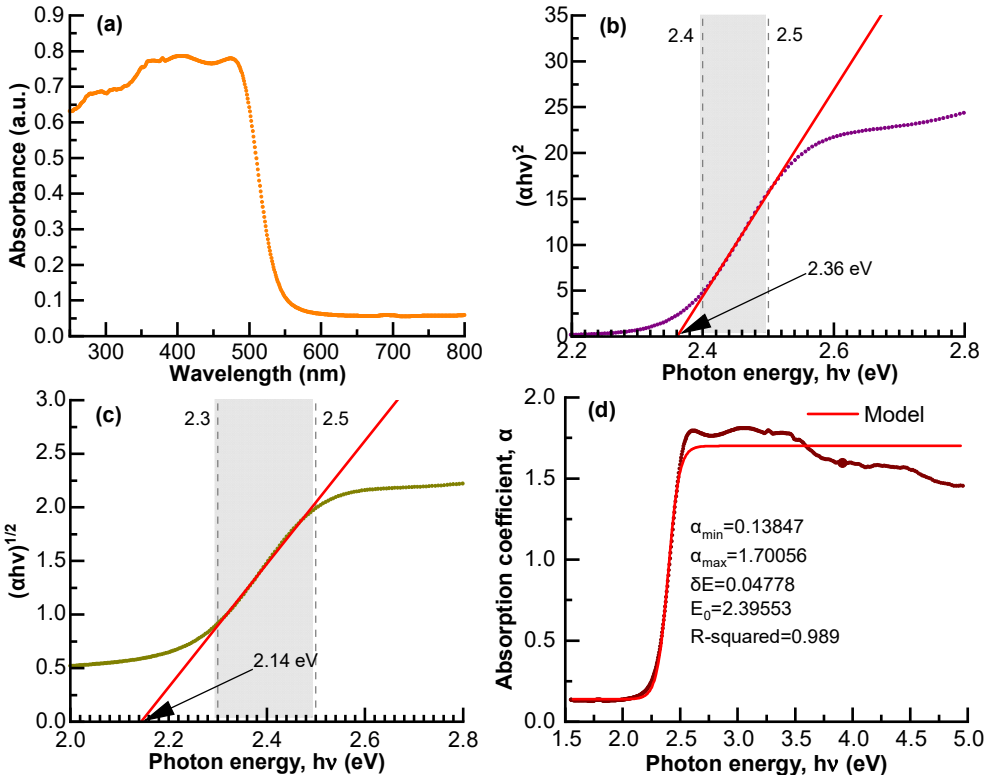

Fig 4. (a) UV-vis absorption spectrum; (b-c) direct and indirect bandgap determined by the modified Tauc plot method; (d) the sigmoid-Boltzmann fit method

solids is bandgap. Fig. 4(a) shows that $BiVO_4$ intensely absorbs visible light. Among various analytical techniques, UV-vis spectrophotometry provides a fast assessment of the bandgap. The Tauc plot method, originally designed for investigating non-direct interband transitions in amorphous bulk semiconductors, uses UV-vis measurement and a simple-power law fit of the absorbance to determine the bandgap. Besides, the modified Tauc plot method, known as "$(\alpha h\nu)^m$ plot" (Eq. (6)), is widely accepted for perfectly crystalline bulk solids.

$$(\alpha h\nu)^m = B\left(h\nu - E_g\right) \quad (6)$$

In Eq. (6), α is the absorption coefficient; h and ν are the Planck constant and photon frequency, respectively; *B* is a constant; E_g is the bandgap; m is equal to ½ or 2 for indirect and direct transition, respectively. The band gap is determined by extrapolating the linear part of the plot to the x-axis, as illustrated in Fig. 4(b-c). The estimated bandgap was about 2.36 and 2.14 eV for direct and indirect transition cases.

However, the accuracy of these methods heavily depends on the selection of the fitting range, as exemplified in Fig. S2, where variation in the fitting range results in discrepancies in the bandgap. This result demonstrates the susceptibility of these methods to human intervention, hence the necessity of an alternative approach to overcome this limitation [47]. A novel method utilizing an entire absorption spectrum rather than a portion thereof has been proposed for determining the bandgap of crystalline materials [48]. The absorption coefficient profile resembles the sigmoid-Boltzmann function (Eq. (7)):

$$\alpha = \alpha_{max} + \frac{\alpha_{min} - \alpha_{max}}{1 + \exp\frac{E - E_0^{Boltzmann}}{\delta E}} \quad (7)$$

where α_{max} and α_{min} are the maximum and minimum absorption coefficients, respectively; $E_0^{Boltzmann}$ is the energy at which α is at the mean of α_{max} and α_{min}; δE is the slope factor of the sigmoid curve. These parameters can be retrieved by fitting the absorption profile with the

sigmoid-Boltzmann function. Fig. 4(d) shows α(E) data was well fitted with the sigmoid-Boltzmann function with $R^2 = 0.98$ and related parameters. In this method, the bandgap is determined by Eq. (8):

$$Eg = E_0^{Boltzman} - n_{dir-ind}^{Boltzman} \times \delta E \quad (8)$$

in which $n_{dir\text{-}ind}^{Boltzmann}$ is an empirical parameter and depends on the type of optical transition ($n_{direct} = 0.3$, $n_{indirect} = 4.3$). Based on the fitting results, the indirect and direct bandgap produced by this method were determined to be 2.19 and 2.38 eV for indirect and direct transition, respectively. By fitting an entire absorption spectrum, this innovative approach holds promise in mitigating the subjective intervention associated with selecting the fitting range, enabling reliable comparison between studies in the future.

Photocatalytic Activity

The catalytic activity of as-prepared samples was assessed via photo-decolorization of methylene blue under a simulated solar irradiation from a low-wattage lamp (26 W). Degradation was monitored by tracking the decrease in absorbance (A), which is proportional to the concentration (C) of MB, as shown in Fig. S4(b). Selecting an appropriate MB concentration is essential to evaluate the photocatalytic activity of as-prepared samples. Three initial concentrations of MB (3, 10, and 20 ppm) were tested with a sample prepared at 200 °C, pH 0.50, 10 h. As shown in Table S5, degradation profiles followed first-order kinetic. The catalyst had superior performance with a solution of 10 ppm, which is also a commonly used concentration in other studies, making comparisons easier. Thus, 10 ppm was chosen to evaluate the photocatalytic activity of the prepared samples. It is suggested that the degradation could be enhanced in alkaline conditions owing to MB's cationic nature. Intriguingly, over half of MB underwent self-degradation at pH level of 12.0 within 90 min of exposure to light, even in the absence of catalysts (Fig. S5). MB can absorb light within the 500–700 nm range, creating singlet and triplet species through electronic transitions and intersystem crossing, and subsequently undergoing self-decomposition. In an alkaline environment, this self-decomposition is enhanced by •OH radicals, which are generated through the reduction of MB radicals by OH^- [49]. To avoid overestimating photocatalytic activity, subsequent experiments were performed at the natural pH level of the solution, which is approximately 6.4.

The influence of hydrothermal temperature on $BiVO_4$'s performance is graphically depicted in Fig. 5(a), which illustrates the relationship between degradation efficacy and synthesis temperature. As shown in Table S6 and Fig. S6, the kinetic rate constant rose from 0.689×10^{-2} to 0.792×10^{-2} min^{-1} as the temperature increased from 150 to 200 °C. However, it diminished significantly to 0.358×10^{-2} min^{-1} when using the sample prepared at 220 °C. These results suggest that hydrothermal temperature has a substantial influence on catalytic activity.

Fig. 5(b) reveals that both the kinetic rate constant and crystal aspect ratio follow the same pattern, where a high (040)/(110) ratio corresponds to high activity. It was found that the mobility of photogenerated electrons is greater in the crystal axis (010) compared to (110), which is opposite the trend for holes [50]. Furthermore, the high aspect ratio of (040)/(110) can lower the energy barrier for charge transfer [51]. Consequently, photogenerated carriers are likely to separate into different planes. Besides, the photo-absorption coefficient along axis (010) was calculated to be weaker than that of (110) in the region beyond 420 nm [52]. Thus, enlarging (040) facets can enhance light absorption capacity. Nevertheless, the extension of (040) facets should be optimized to prevent rapid charge separation caused by the unbalanced distribution of photogenerated carriers [53].

The crystal aspect ratio of (040)/(110) influences the conduction band (CB) and valence band (VB) edge energies of the material. An increase in this ratio results in a negative shift in both CB and VB, enhancing reduction capability [51]. However, rising temperature intensifies compressive strain, lifting the VB upward but barely affecting the CB [26], lowering oxidation potential and reducing photocatalytic performance. Besides, increasing temperature creates more defects, such as dislocations, acting as recombination centers of photogenerated carriers [41-42]. Therefore, the worst

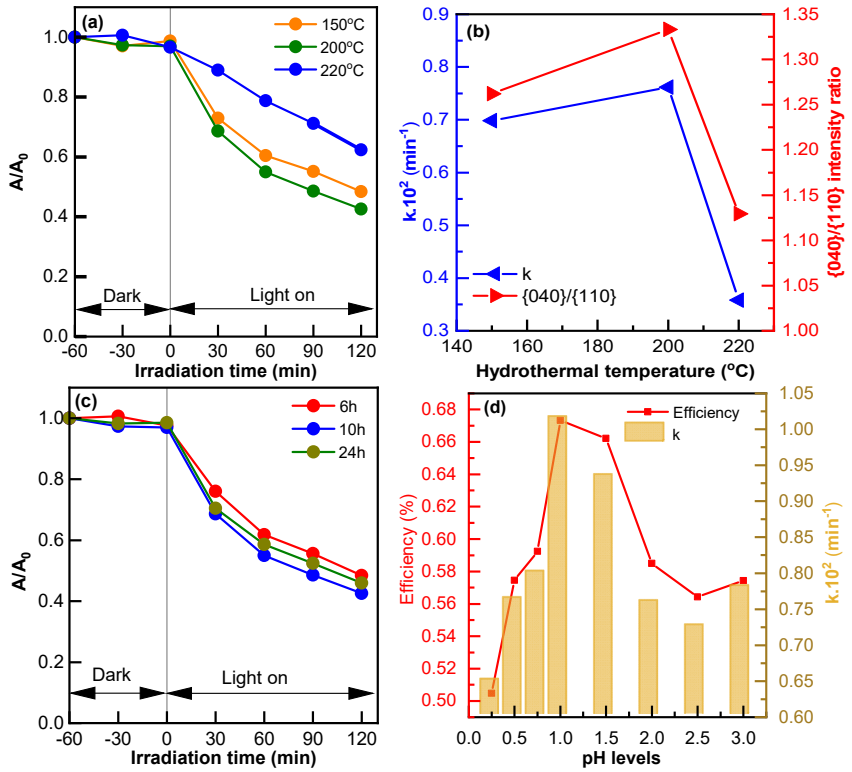

Fig 5. (a) Decay profile of MB using samples prepared at different hydrothermal temperatures; (b) the impact of (040)/(110) ratio on the photocatalytic activity; (c) decay profile of MB using samples prepared at different hydrothermal treatment duration; (d) the effect of pH levels during hydrothermal stage on the photocatalytic activity

performance of the sample synthesized at 220 °C correlates to its modest (040)/(110) ratio, large compressive strain, and significant defect presence. Additionally, the temperature also affects the material's bandgap. Unlike several classical semiconductors, volume contraction causes a decrease in bandgap energy in $BiVO_4$ [26], with $\Delta E_g = \alpha_V \frac{\Delta V}{V}$ (where α_V and $\Delta V/V$ describe the material's bandgap deformation potential and change in unit cell volume, respectively) [32]. Moreover, volume contraction causes the enhanced hybridization between Bi 6s and O 2p orbitals, thus improving charge separation as discussed previously. Among the three samples, the one prepared at 200 °C, which possesses a high degree of [040] exposed facet, small unit cell volumes, exhibited superior performance.

Turning to the hydrothermal duration, a 10-h treatment emerged as optimal for enhancing the photocatalytic activity (Fig. 5(c)). Table S6 shows that prolonging hydrothermal duration correlated with the increase in rate constant, achieving approximately 0.762×10^{-2} min^{-1} for the sample treated for 10 h. The monoclinic phase of $BiVO_4$ (m-$BiVO_4$), synthesized using hydrothermal method, was found to predominate after 4 h, and reached its peak at 10 h [24]. There was a minimal change in the phase composition beyond 10 h [24]. Since the photoactivity of m-$BiVO_4$ is closely associated with phase compositions, the improvement in activity observed in the sample treated for 10 h is likely attributed to changes in the monoclinic phase. However, the degradation rate constant slightly decreased to 0.70×10^{-2} min^{-1} when the time was set at 24 h. As the holding time increases, the (040) facet continues to develop, possibly resulting in a decrease in the proportion of (040) facet. Furthermore, extending the duration of hydrothermal treatment may lead to coalescence, where larger particles consume smaller ones via the Ostwald ripening mechanism, reducing the surface area and adversely affecting activity [54].

The remaining hydrothermal parameter to consider is the pH level. A discernible disparity in behavior emerged across various pH levels ranging from 0.25 to 3.00. As shown in Fig. 5(d) and Table S6, there is a pronounced enhancement in both the decolorization percentage and the kinetic rate constant as the pH level increased from 0.25 to 1.00. Specifically, the kinetic rate constant, initially estimated at 0.648×10^{-2} min^{-1} for the sample prepared at pH 0.25, reached its zenith of 1.015×10^{-2} min^{-1} at pH 1.0. Under optimal synthesis conditions (pH 1.00), crystals possess less compressive strain and larger domain size (Table 2) compared to the sample synthesized at pH 0.50. Fig. 1(d) reveals that the sample prepared at pH 1.0 possessed a more extensive (040) facet (i.e., $I_{040}/I_{110} = 1.54$) relative to its pH 0.5 counterpart (i.e., $I_{040}/I_{110} = 1.33$ (Fig. 1(b))), despite their shared polyhedral morphology (Fig. 3(a-b)). The shape of crystals significantly affects charge carrier dynamics. Facet-engineered $BiVO_4$ samples demonstrated a 30-fold increase in the accumulation of long-lived holes and a 5-fold increase in their lifetime compared to non-faceted control $BiVO_4$ samples [55]. Notably, in this study, the polyhedral morphology entirely collapsed and transformed into a rod-like shape at pH 2.0 (Fig. 3(c)). Coincidentally, further increasing the pH level also caused a marked decline in catalytic activity, suggesting a reduction in charge separation. Once again, these results reinforce the pivotal role of polyhedral morphology, as well as (040) facet extent, in enhancing photocatalytic activity.

$BiVO_4$ is a compelling candidate for photocatalysis due to its small band gap energy. In recent studies, TiO_2 synthesized by hydrolysis method exhibits a decolorization percentage of merely 32.5% ($k = 0.325 \times 10^{-2}$ min^{-1}) [56]. TiO_2 itself requires modification to achieve higher activity. For instance, Cu-doped TiO_2 can achieve up to 92.31% decolorization ($k = 1.01 \times 10^{-2}$ min^{-1}) after 4 h of illumination [56]. A comparative analysis of photocatalytic activity, detailed in Table S7, unequivocally demonstrates the competitive ability of the as-prepared $BiVO_4$ catalyst relative to both $BiVO_4$-based and other recent photocatalyst counterparts. This exceptional performance is rendered by a simple synthesis process, which does not require additional surfactants or directing agents, thereby lowering the material and fabrication costs. More importantly, catalyst's capacity to achieve efficient degradation under the illumination of a lower-wattage lamp at the laboratory scale, implies a more substantial performance in larger-scale applications.

■ CONCLUSION

In summary, the facile hydrothermal synthesis method yields monoclinic phase $BiVO_4$ with desirable characteristics without surfactants or directing agents. By adjusting the hydrothermal parameters, the morphology can be tuned with a greater extent of (040) facet-enhancing photocatalytic activity. However, compressive strain introduced during synthesis can negatively impact the photocatalytic activity. Reducing non-uniform compressive strain and severe defects such as dislocation is crucial for optimization. The sample synthesized at 200 °C and pH 1.0, with 10 h of hydrothermal treatment, outperformed others, achieving 67% MB removal within 120 min under irradiation, with a kinetic rate of 1.015×10^{-2} min^{-1}. The simplicity of this synthesis method, combined with its high performance even under low-power lamp illumination, holds promise for practical applications and potential scalability.

■ ACKNOWLEDGMENTS

We acknowledge Ho Chi Minh City University of Technology (HCMUT), VNU-HCM for supporting this study.

■ CONFLICT OF INTEREST

The authors declare no conflict of interest.

■ AUTHOR CONTRIBUTIONS

All authors influenced the conceptualization and methodology of the study. Vinh-Tien Truong conducted material synthesis, data analysis, visualization, and prepared an original draft. Pham-Ngoc-My Le supported the investigation and conducted revisions. Minh-Vien Le served as supervisor, led the conceptualization and writing-review. The completed work was read and approved by all authors.

■ REFERENCES

[1] Boretti, A., and Rosa, L., 2019, Reassessing the projections of the World Water Development Report, *npj Clean Water*, 2 (1), 15.

[2] Desore, A., and Narula, S.A., 2018, An overview on corporate response towards sustainability issues in textile industry, *Environ. Dev. Sustainability*, 20 (4), 1439–1459.

[3] Fito, J., Abewaa, M., Mengistu, A., Angassa, K., Ambaye, A.D., Moyo, W., and Nkambule, T., 2023, Adsorption of methylene blue from textile industrial wastewater using activated carbon developed from *Rumex abyssinicus* plant, *Sci. Rep.*, 13 (1), 5427.

[4] Malathi, A., Madhavan, J., Ashokkumar, M., and Arunachalam, P., 2018, A review on $BiVO_4$ photocatalyst: Activity enhancement methods for solar photocatalytic applications, *Appl. Catal., A*, 555, 47–74.

[5] Drisya, K.T., Solís-López, M., Ríos-Ramírez, J.J., Durán-Álvarez, J.C., Rousseau, A., Velumani, S., Asomoza, R., Kassiba, A., Jantrania, A., and Castaneda, H., 2020, Electronic and optical competence of TiO_2/$BiVO_4$ nanocomposites in the photocatalytic processes, *Sci. Rep.*, 10 (1), 13507.

[6] Kamble, G.S., and Ling, Y.C., 2020, Solvothermal synthesis of facet-dependent $BiVO_4$ photocatalyst with enhanced visible-light-driven photocatalytic degradation of organic pollutant: Assessment of toxicity by zebrafish embryo, *Sci. Rep.*, 10 (1), 12993.

[7] Rather, R.A., Mehta, A., Lu, Y., Valant, M., Fang, M., and Liu, W., 2021, Influence of exposed facets, morphology and hetero-interfaces of $BiVO_4$ on photocatalytic water oxidation: A review, *Int. J. Hydrogen Energy*, 46 (42), 21866–21888.

[8] Wang, S., Wan, K., Feng, J., Yang, Y., and Wang, S., 2025, $BiVO_4$ photoanodes with enhanced photoelectrochemical performance: Preparation, modification and emerging applications, *J. Mater. Sci. Technol.*, 217, 182–220.

[9] Chen, X., Dong, Q., Chen, S., Zhang, Z., Zhang, X., Di, Y., Jiang, A., Zhang, D., and Li, T., 2023, Halloysite nanotubes supported $BiVO_4$/$BaSnO_3$ p-n heterojunction photocatalysts for the enhanced degradation of methylene blue under visible light, *Colloids Surf., A*, 664, 131143.

[10] Tran, T.H., Le, P.N.M., Ngo, T.H., Huynh, N.D.T., Oh, W.C., and Le, M.V., 2024, An investigation on the visible-light-driven Z-scheme $BiVO_4$/g-C_3N_4 heterostructures: Performance, evaluation, and mechanism for dye and antibiotics degradation, *Mater. Today Commun.*, 40, 109373.

[11] Mohamed, A.M., Abdelwahab, S.M., Elsawy, N.M., Ahmed, N.A., and Raafat, A.I., 2024, E-beam irradiation-induced synthesis of hydroxyethyl cellulose/(Cu_2O-rGO)/$BiVO_4$-based nanocomposite for photocatalytic remediation of wastewater under visible light, *Int. J. Biol. Macromol.*, 258, 128681.

[12] Prabhavathy, S., and Arivuoli, D., 2022, Visible light-induced silver and lanthanum co-doped $BiVO_4$ nanoparticles for photocatalytic dye degradation of organic pollutants, *Inorg. Chem. Commun.*, 141, 109483.

[13] Xu, X., Du, M., Chen, T., Xiong, S., Wu, T., Zhao, D., and Fan, Z., 2016, New insights into Ag-doped $BiVO_4$ microspheres as visible light photocatalysts, *RSC Adv.*, 6 (101), 98788–98796.

[14] Pham, M.Q., Ngo, T.M., Nguyen, V.H., Nong, L.X., Vo, D.V.N., Tran, T.V., Nguyen, T.D., Bui, X.T., and Nguyen, T.D., 2020, Facile solvothermal synthesis of highly active monoclinic scheelite $BiVO_4$ for photocatalytic degradation of methylene blue under white LED light irradiation, *Arabian J. Chem.*, 13 (11), 8388–8394.

[15] Wang, D., Jiang, H., Zong, X., Xu, Q., Ma, Y., Li, G., and Li, C., 2011, Crystal facet dependence of water oxidation on $BiVO_4$ sheets under visible light irradiation, *Chem. - Eur. J.*, 17 (4), 1275–1282.

[16] Liu, J., Li, B., Kong, L., Xiao, Q., and Huang, S., 2023, Surfactants-assisted morphological regulation of $BiVO_4$ nanostructures for photocatalytic degradation of organic pollutants in wastewater, *J. Phys. Chem. Solids*, 172, 111079.

[17] Zhu, M., Yang, S., Wang, D., Hogan, J., and Sadrzadeh, M., 2024, CTAC-assisted monoclinic $BiVO_4$ with oxygen defects for efficient photocatalytic performances: A combined

experimental and DFT study, *J. Alloys Compd.*, 990, 174404.

[18] Liu, M., Zheng, L., Deng, J., Gao, J., Su, K., Sheng, X., He, J., Feng, D., Guo, L., Chen, C., and Li, Y., 2023, Construction of Ag nanoparticle decorated AgBr/$BiVO_4$ shell/core structure plasmonic photocatalysts towards high photocatalytic elimination of contaminations under visible light, *J. Alloys Compd.*, 931, 167584.

[19] Baral, B., and Parida, K., 2020, {040/110} Facet isotype heterojunctions with monoclinic scheelite $BiVO_4$, *Inorg. Chem.*, 59 (14), 10328–10342.

[20] Yang, Y., Gong, K., Shi, Q., Wu, X., Li, K., Tong, X., Li, J., Zhang, L., Wang, X., Li, B., Bao, X., and Meng, S., 2024, Facet-dependent Fe_2O_3/$BiVO_4$(110)/$BiVO_4$(010)/Fe_2O_3 dual S-scheme photocatalyst as an efficient visible-light-driven peroxymonosulfate activator for norfloxacin degradation, *Langmuir*, 40 (17), 9155–9169.

[21] Wang, H., Liu, X., Wu, D., Zhao, Y., Li, N., Li, Y., Fan, X., Xia, Q., Zhang, F., and Peng, W., 2023, Role variations of MnOx on monoclinic $BiVO_4$ (110)/(040) facets for enhanced Photo-Fenton reactions, *J. Colloid Interface Sci.*, 646, 219–227.

[22] Hu, Y., Gao, Y., Liu, F., Tian, Y., Wang, Q., Zeng, D., Shen, T., Song, J., Guan, R., and Yuan, H., 2023, The {010} and {110} facets of $BiVO_4$ were selectively modified by Cu and g-C_3N_4 to enhance its visible light photocatalytic performance, *Sep. Purif. Technol.*, 323, 124471.

[23] de Matos Rodrigues, M.H., Borges, K.C.M., Tello, A.C.M., Roca, R.A., de Fátima Gonçalves, R., da Silva, A.B.F., Longo, E., and Godinho, M.J., 2023, Effect of pH on the synthesis of $BiVO_4$ to improve photocatalysis and antimicrobial properties, *Mater. Chem. Phys.*, 296, 127198.

[24] Zhao, Y., Li, R., Mu, L., and Li, C., 2017, Significance of crystal morphology controlling in semiconductor-based photocatalysis: A case study on $BiVO_4$ photocatalyst, *Cryst. Growth Des.*, 17 (6), 2923–2928.

[25] Guo, Y., Wei, X., Zhang, K., Zhang, J., Mi, L., Wu, Z., Wang, G., Li, Y., Huang, Q., Fu, W., Zhang, Y., Hou, A., Wang, H., and Qi, X., 2023, Study on the growth mechanism of dispersed monoclinic $BiVO_4$ in hydrothermal process and its photocatalytic activity, *J. Dispersion Sci. Technol.*, 44 (9), 1549–1561.

[26] Choi, M., 2021, Photocatalytic and photoelectrochemical activities of strained $BiVO_4$, *Appl. Phys. Lett.*, 118 (16), 161901.

[27] Xie, S., Shen, Z., Zhang, H., Cheng, J., Zhang, Q., and Wang, Y., 2017, Photocatalytic coupling of formaldehyde to ethylene glycol and glycolaldehyde over bismuth vanadate with controllable facets and cocatalysts, *Catal. Sci. Technol.*, 7 (4), 923–933.

[28] Zheng, L.L., Tian, L., Wang, D., Chen, Y., Tang, Q.Q., Xing, Q.J., Liu, X.Z., Wu, D.S., and Zou, J.P., 2023, Facet engineering of $BiVO_4$ photocatalyst for the synergetic adsorption and activation of persulfate for organic pollutants degradation, *Chem. Eng. J.*, 473, 145507.

[29] Mezyen, M., El Fidha, G., Bitri, N., Harrathi, F., Ly, I., and Llobet, E., 2023, Visible light activated SnO_2:Dy thin films for the photocatalytic degradation of methylene blue, *RSC Adv.*, 13 (44), 31151–31166.

[30] Song, Y., Liu, Y., and Ou, X., 2020, Heat-rate-controlled hydrothermal crystallization of high-performance $LiMn_{0.7}Fe_{0.3}PO_4$ cathode material for lithium-ion batteries, *Ceram. Int.*, 46 (4), 5069–5076.

[31] Dolabella, S., Borzì, A., Dommann, A., and Neels, A., 2022, Lattice strain and defects analysis in nanostructured semiconductor materials and devices by high-resolution X-ray diffraction: Theoretical and practical aspects, *Small Methods*, 6 (2), 2100932.

[32] Fernandez, E.N., van de Krol, R., and Abdi, F.F., 2024, Tuning the optical and photoelectrochemical properties of epitaxial $BiVO_4$ by lattice strain, *Small Struct.*, 2400097.

[33] Ozaki, Y., Suzuki, Y., Hawai, T., Saito, K., Onishi, M., and Ono, K., 2020, Automated crystal structure analysis based on blackbox optimisation, *npj Comput. Mater.*, 6 (1), 75.

[34] Riemke, F.C., Ücker, C.L., Rangel, E.M., Cozza, L., Almeida, S.L., Ferrer, M.M., Cava, S., L.V. Carreno, N., Ceretta, E., and Raubach, C.W., 2023, Theoretical

and experimental photocatalytic implications of Co ions upon the $SrTiO_3$ lattice, *Chem. Phys.*, 567, 111772.

[35] Manh, D.H., Ngoc Nha, T.T., Hong Phong, L.T., Nam, P.H., Thanh, T.D., and Phong, P.T., 2023, Determination of the crystalline size of hexagonal $La_{1-x}Sr_xMnO_3$ (x = 0.3) nanoparticles from X-ray diffraction - A comparative study, *RSC Adv.*, 13 (36), 25007–25017.

[36] Li, Z., Chen, X., Wang, L., Xiao, M., Shang, Y., Han, W., and Lv, Y., 2023, Photo-induced surface oxygen vacancies for effective promotion of the photocatalytic properties over hierarchical layered $Bi_2O_2(OH)NO_3$, *Chem. Phys.*, 575, 112081.

[37] Langford, J.I., 1992, The use of the Voigt function in determining microstructural properties from diffraction data by means of pattern decomposition, *NIST Spec. Publ.*, 846, 110–126.

[38] Motevalizadeh, L., Heidary, Z., and Abrishami, M.E., 2014, Facile template-free hydrothermal synthesis and microstrain measurement of ZnO nanorods, *Bull. Mater. Sci.*, 37 (3), 397–405.

[39] Muhammed Shafi, P., and Chandra Bose, A., 2015, Impact of crystalline defects and size on X-ray line broadening: A phenomenological approach for tetragonal SnO_2 nanocrystals, *AIP Adv.*, 5 (5), 057137.

[40] Igenepo John, K., Abdul Adenle, A., Timothy Adeleye, A., Pearl Onyia, I., Amune-Matthews, C., and Omorogie, M.O., 2021, Unravelling the effect of crystal dislocation density and microstrain of titanium dioxide nanoparticles on tetracycline removal performance, *Chem. Phys. Lett.*, 776, 138725.

[41] Zafar, Z., Yi, S., Li, J., Li, C., Zhu, Y., Zada, A., Yao, W., Liu, Z., and Yue, X., 2022, Recent development in defects engineered photocatalysts: An overview of the experimental and theoretical strategies, *Energy Environ. Mater.*, 5 (1), 68–114.

[42] Zhang, E., Zhang, M., and Kato, M., 2024, Effect of dislocations on carrier recombination and photoelectrochemical activity in polished and unpolished TiO_2 and $SrTiO_3$ crystals, *J. Appl. Phys.*, 135 (4), 045102.

[43] Jo, W.J., Kang, H.J., Kong, K.J., Lee, Y.S., Park, H., Lee, Y., Buonassisi, T., Gleason, K.K., and Lee, J.S., 2015, Phase transition-induced band edge engineering of $BiVO_4$ to split pure water under visible light, *Proc. Natl. Acad. Sci. U. S. A.*, 112 (45), 13774–13778.

[44] Hill, C., Weber, M.C., Lehmann, J., Leinen, T., Fiebig, M., Kreisel, J., and Guennou, M., 2020, Role of the ferroelastic strain in the optical absorption of $BiVO_4$, *APL Mater.*, 8 (8), 081108.

[45] Tan, G., Zhang, L., Ren, H., Wei, S., Huang, J., and Xia, A., 2013, Effects of pH on the hierarchical structures and photocatalytic performance of $BiVO_4$ powders prepared via the microwave hydrothermal method, *ACS Appl. Mater. Interfaces*, 5 (11), 5186–5193.

[46] Wang, X., Mu, B., Zhang, A., An, X., and Wang, A., 2019, Effects of different pH regulators on the color properties of attapulgite/$BiVO_4$ hybrid pigment, *Powder Technol.*, 343, 68–78.

[47] Jubu, P.R., Danladi, E., Ndeze, U.I., Adedokun, O., Landi, S., Haider, A.J., Adepoju, A.T., Yusof, Y., Obaseki, O.S., and Yam, F.K., 2024, Comment about the use of unconventional Tauc plots for bandgap energy determination of semiconductors using UV–vis spectroscopy, *Results Opt.*, 14, 100606.

[48] Zanatta, A.R., 2024, Temperature-dependent optical bandgap of TiO_2 under the anatase and rutile phases, *Results Phys.*, 60, 107653.

[49] Khan, I., Saeed, K., Zekker, I., Zhang, B., Hendi, A.H., Ahmad, A., Ahmad, S., Zada, N., Ahmad, H., Shah, L.A., Shah, T., and Khan, I., 2022, Review on methylene blue: Its properties, uses, toxicity and photodegradation, *Water*, 14 (2), 242.

[50] Liu, G., Zhu, Y., Yan, Q., Wang, H., Wu, P., Shen, Y., and Doekhi-Bennani, Y., 2021, Tuning electron transfer by crystal facet engineering of $BiVO_4$ for boosting visible-light driven photocatalytic reduction of bromate, *Sci. Total Environ.*, 762, 143086.

[51] Kim, C.W., Ji, S., Kang, M.J., Park, H., Li, F., Cheng, H.M., and Kang, Y.S., 2019, Energy band edge

alignment of anisotropic $BiVO_4$ to drive photoelectrochemical hydrogen evolution, *Mater. Today Energy*, 13, 205–213.

[52] Yang, J., Wang, D., Zhou, X., and Li, C., 2013, A theoretical study on the mechanism of photocatalytic oxygen evolution on $BiVO_4$ in aqueous solution, *Chem. - Eur. J.*, 19 (4), 1320–1326.

[53] Liu, X., Miao, X., Zhang, X., Wang, Y., and Zhu, T., 2023, Influence of crystal planes exposure ratio on photocatalytic and antimicrobial properties of m-$BiVO_4$ under LED visible light, *Inorg. Chem. Commun.*, 148, 110357.

[54] Neto, N.F.A., Nunes, T.B.O., Li, M., Longo, E., Bomio, M.R.D., and Motta, F.V., 2020, Influence of microwave-assisted hydrothermal treatment time on the crystallinity, morphology and optical properties of $ZnWO_4$ nanoparticles: Photocatalytic activity, *Ceram. Int.*, 46 (2), 1766–1774.

[55] He, T., Zhao, Y., Benetti, D., Moss, B., Tian, L., Selim, S., Li, R., Fan, F., Li, Q., Wang, X., Li, C., and Durrant, J.R., 2024, Facet-engineered $BiVO_4$ photocatalysts for water oxidation: Lifetime gain versus energetic loss, *J. Am. Chem. Soc.*, 146 (39), 27080–27089.

[56] Zakir, O., Ait-Karra, A., Idouhli, R., Khadiri, M., Dikici, B., Zegzouti, A., Abouelfida, A., and Outzourhit, A., 2025, A study on the influence of metal Ag, Cu, and Fe doping on the morphological, structural, and photocatalytic activity of TiO_2 nanostructures, *J. Alloys Compd.*, 1010, 177141.